

From Planetesimals to Dwarf Planets by Pebble Accretion

Chris W. Ormel¹, Yukun Huang (黄宇坤)^{1,2}

¹ Department of Astronomy, Tsinghua University, Beijing 100084, China
e-mail: chrisormel@tsinghua.edu.cn

² National Astronomical Observatory of Japan, 2-21-1 Osawa, Mitaka, Tokyo 181-8588, Japan

February 7, 2025

ABSTRACT

The size distribution of trans-Neptunian objects (TNOs) in the Kuiper Belt provides crucial insights into the formation and evolution of the outer Solar System. Recent observational surveys, including OSSOS++, have revealed that dynamically cold and hot TNO populations exhibit similar size distributions for dimmer objects ($H_r > 5$), which are consistent with planetesimal formation by streaming instability (SI). However, the hot population contains a significantly larger number of massive bodies, including several dwarf planets. In this study, we investigate the role of pebble accretion in shaping the size distribution of hot TNOs, after their formation in the primordial disk (PB) between 20 and 30 au and before these bodies were dynamically implanted into their current orbits by a migrating Neptune. We find that pebble accretion grows the most massive bodies only, consistent with the flattening of the distribution brightwards of $H_r = 5$. All results point to a correlation (degeneracy) between the pebble aerodynamic size and the intensity of the gas motions. Nevertheless, accretion from an inward-drifting stream of pebbles is unlikely, as it puts extreme demands on the mass budget of pebbles. In particular, the masses of the cold classicals are too low to trigger pebble accretion. Accretion in an environment where pebbles are entrained, as believed to be the case in ALMA rings, is preferable. Combining the constraints obtained from this study with ALMA imagery morphology fitting reveals a typical pebble aerodynamic size of $\tau_s \sim 10^{-2}$, a turbulent diffusivity parameter $\alpha_D \sim 10^{-3}$, and a total accreted pebble mass of $\sim 10 m_\oplus$ in the primordial belt. Those TNOs formed through significant pebble accretion with masses exceeding $\sim 10^{-4} m_\oplus$ are likely to satisfy the International Astronomical Union’s “round shape” criterion for dwarf planets.

Key words. Planetary systems – Planets and satellites: composition – Planets and satellites: formation – Planets and satellites: physical evolution – Planet-disk interactions – Methods: numerical

1. Introduction

The trans-Neptunian space, conventionally known as the Kuiper belt, hosts numerous icy bodies which are believed to be ancient remnants of the solar system’s outer planetesimal disk. As more trans-Neptunian objects (TNOs) are discovered by various modern observational surveys, such as the Canada–France Ecliptic Plane Survey (CFEPS; Jones et al. 2006), the Deep Ecliptic Survey (DES; Adams et al. 2014), the Outer Solar System Origins Survey (OSSOS; Bannister et al. 2018), the Dark Energy Survey (DES; Bernardinelli et al. 2022), and the DECam Ecliptic Exploration Project (DEEP; Trilling et al. 2024), there is a growing consensus that the Kuiper belt consists of two distinct populations: dynamically cold TNOs, formed in-situ (~ 45 au), and dynamically hot TNOs, which are believed to have formed closer to the Sun (~ 20 au), before being implanted to their current locations.

Cold TNOs, also known as cold classicals, are characterized by their low inclinations and relatively stable orbits, suggesting they formed in their current locations and have remained dynamically cold (Petit et al. 2011). In contrast, hot TNOs, which include the hot classicals, resonant objects, and scattering disk objects (see Gladman et al. 2008 for definitions of TNOs dynamical classes), exhibit higher inclinations and eccentricities, suggesting a more violent dynamical history. Moreover, cold TNOs tend to have redder colors, indicating a different surface composition and evolution history compared to the more neutral colors of hot TNOs (Doressoundiram et al. 2002; Trujillo & Brown

2002; Pike & Lawler 2017; Schwamb et al. 2019; Müller et al. 2020; Fernández-Valenzuela et al. 2021). The binary fraction is also higher among cold TNOs (Noll et al. 2020), especially those with comparable sizes. Additionally, dwarf planet-sized TNOs are predominantly found in the hot populations, with cold TNOs lacking large objects (Brown 2008; Fraser et al. 2014). All these differences—orbital characteristics, colors, binary fractions, and size distributions—support the hypothesis that cold and hot TNOs formed at different radial locations and experienced different dynamical evolutions. Cold TNOs likely formed in-situ at their current locations, while hot TNOs formed closer to the Sun and were subsequently implanted into their current orbits during the migration of the giant planets (Malhotra 1993; Gomes 2003; Levison et al. 2008; Nesvorný 2015).

The implantation process of hot TNOs is closely linked to the planetesimal-driven migration of the giant planets, particularly Neptune. In this hypothesis, Neptune is believed to have formed closer to the Sun and migrated outward into a primordial planetesimal belt that spanned ~ 20 – 30 au (Gomes 2003; Levison et al. 2008), with a total estimated mass of $\sim 20 m_\oplus$ (Nesvorný 2015). Most of the planetesimals were scattered inward consecutively by Neptune, Uranus, and Saturn, until their orbits cross the orbit of Jupiter. The strong gravity of Jupiter effectively ejected the vast majority of these planetesimals out of the Solar System, leaving only a small fraction to form the Jupiter Trojans (Morbidelli et al. 2005; Nesvorný et al. 2013). Another fraction of the planetesimals were scattered outward by a migrating Neptune

into the trans-Neptunian region, forming the hot or implanted population (Malhotra 1993; Nesvorný et al. 2016).

As the number of discovered TNOs continues to grow, the size distribution¹ of both cold and hot TNOs is becoming increasingly well-constrained. Kavelaars et al. (2021) reported the H_r distribution of the cold classical belt from $H_r \approx 5$ to 12 detected by OSSOS, and found an exponentially tapered power-law with an index of $\alpha \approx 0.4$. This functional form is also consistent with the DEEP survey (Napier et al. 2024). Recently, streaming instability (SI) has emerged as one of the leading theories for planetesimal formation in the solar nebula, as evidenced by the high binary fractions observed in cold classicals (Nesvorný et al. 2010, 2019), and the discoveries of contact binaries such as Arrokoth (McKinnon et al. 2020; Lyra et al. 2021). The exponentially tapered power-law is also consistent with SI simulations that model the planetesimal formation process (Schäfer et al. 2017; Abod et al. 2019).

In a follow-up study of the OSSOS++ survey, Petit et al. (2023) conducted a similar analysis for the hot belt. They found that the shape of the H_r distribution of the hot belt is similar to that of the cold belt, ranging from $H_r \approx 5$ to $H_r \approx 8.3$ (corresponding roughly to bodies with $D \approx 90$ km in diameter²). This upper limit corresponds to the sensitivity threshold of the OSSOS++ survey at ~ 48 au, given an apparent magnitude limit of $m_r \approx 25$. They also found that the all dynamically hot TNOs and those limited to the main belt exhibit remarkably similar H_r distributions (see Figure 3 in Petit et al. 2023), further supporting the shared origin of the dynamically hot TNOs. Given the similarity in the size distributions of the cold and hot TNOs in the low mass end ($H_r \gtrsim 5$, roughly $D \gtrsim 400$ km), it is natural to postulate that both populations started off with a similar initial mass function (IMF) given by the SI process. In contrast, the (future) hot population had the high mass end altered by other planet formation processes.

Here, we postulate that the process that affected the high-mass end of the size distribution of bodies in the primordial belt has been pebble accretion. A similar suggestion has recently been made by Cañas et al. (2024). Pebble accretion is a process that takes place in a gas-rich disks and involves small particles that are aerodynamically coupled to the gas (Ormel & Klahr 2010; Lambrechts & Johansen 2012). Pebble accretion has been widely used to model the growth of planetary bodies in the solar and exoplanet systems (Liu & Ji 2020; Drążkowska et al. 2023). Invoking pebble accretion to explain the flattening of the TNO size distribution at high mass is attractive, as pebble accretion operates on bodies above a certain mass scale (Ormel 2017).

The process that is envisioned is schematically illustrated in Figure 1. SI forms bodies that follow a tapered-exponential in both the cold and the primordial belts. But only the primordial belt featured conditions for pebble accretion to materialize. While the size distribution of smaller bodies stays intact and continuous to follow the initial mass function (IMF) bodies obtain after SI, the larger bodies consume pebbles. Afterwards, the dynamical instability implanted these bodies into the trans-Neptunian space.

Pebble accretion is sensitive to the physical properties of the particles, as well as the local disk conditions. Two parameters in particular are responsible for the characteristics of the accretion:

¹ The absolute magnitude measured with the r filter (H_r) is often used as a handle to study the size of TNOs. For the conversion between H_r and TNO mass, see Section 2.1 and Appendix A.

² The relation between the H_r magnitude, mass, and diameter is detailed in Appendix A. When quoting diameters, a nominal internal density of 1 g cm^{-3} is assumed.

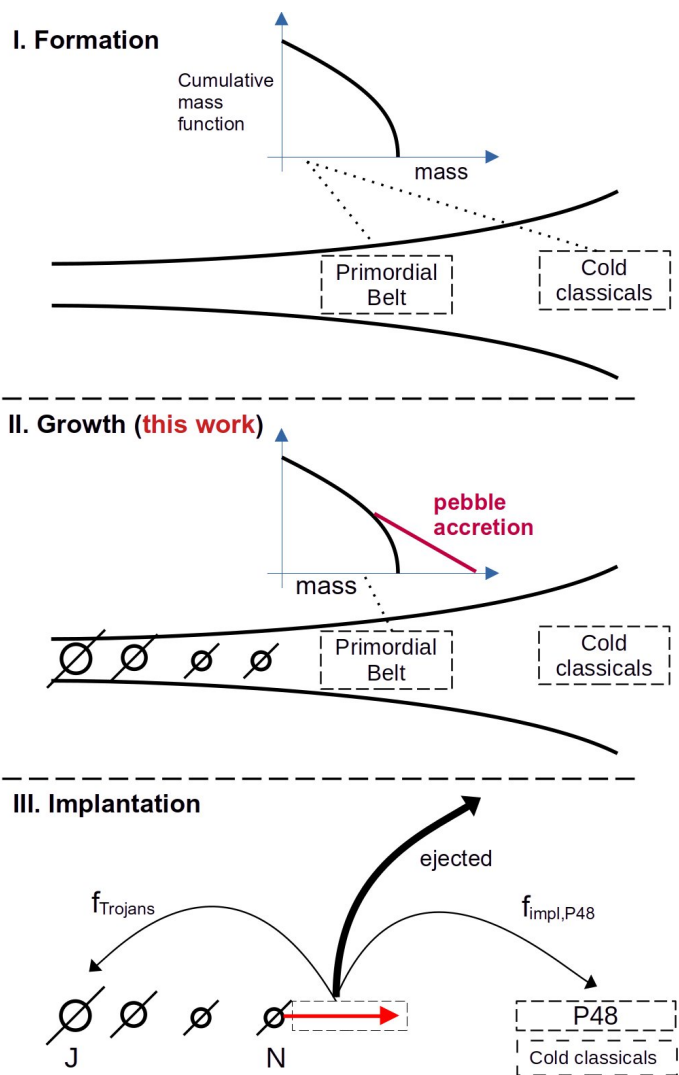


Fig. 1. Envisioned chronology of the formation of trans-Neptunian objects (TNOs). **I. Formation.** An initial burst of planetesimal formation populates bodies in the primordial belt (PB) at ~ 20 au and the cold classicals (CC) at ~ 40 – 50 au. It is assumed that the *shape* of the cold classicals and the primordial belt size distributions are similar, both featuring a tapered exponential at high mass. **II. Growth:** Pebble accretion, acting preferentially on the massive bodies, alters the size distribution of the PB. Growth takes place in a gas-rich medium. This is the phase investigated in this work. **III. Implantation.** Neptune’s migration disperses the PB with an implantation fraction $f_{\text{impl,P48}}$ populating the dynamically hot bodies within 48 au (population P48).

the particle aerodynamic size τ_s and the velocity Δv at which pebbles approach the planetary body. In this work, we conduct a quantitative study to verify which combination of these and other parameters are consistent with the size distribution of current TNOs. To this effect, we carefully select a sample of TNOs that are complete, based on the OSSOS++ survey and the Minor Planet Center (MPC) database. For simplicity, we limit the number of parameters in our model (e.g., we only treat one particle size). As one of our key results, we find a tight relation between pebble aerodynamic size τ_s and relative velocity Δv , which favors formation in an environments that resemble the azimuthally symmetric structures seen in ALMA imagery (Bae et al. 2023), commonly referred to as "ALMA rings".

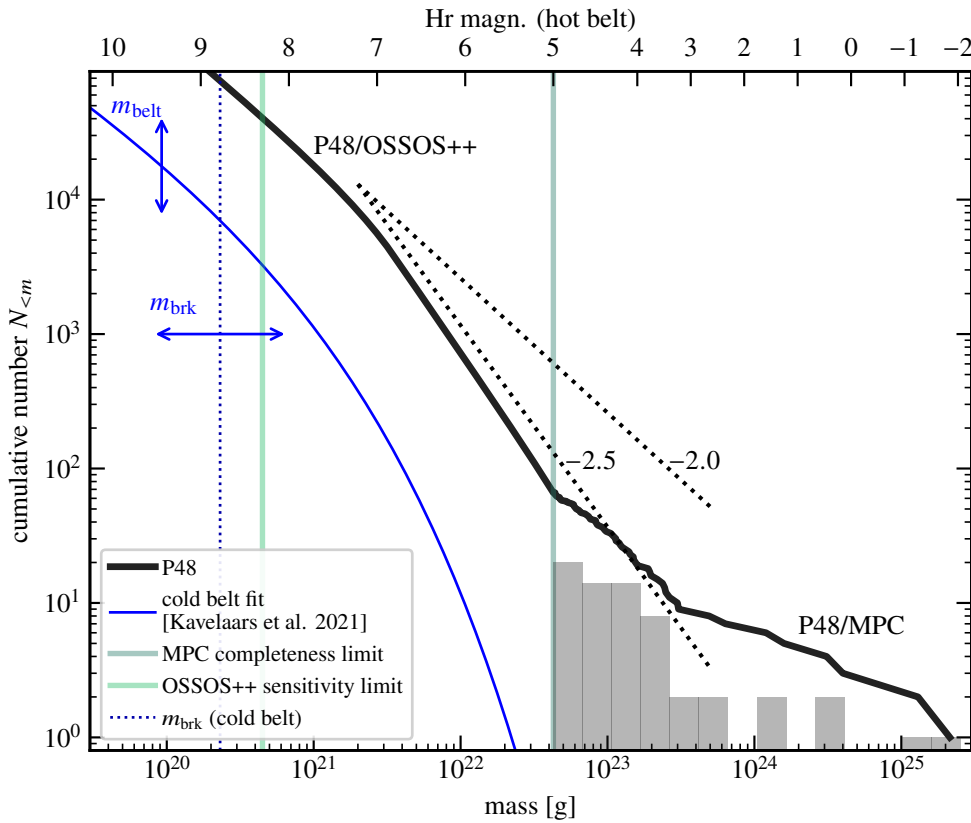


Fig. 2. Cumulative number distribution ($N_{<m}$) of bodies in the cold belt and the dynamical hot P48. The cold belt is well described by the analytical fit of Kavelaars et al. (2021) (Equation (2)), whose shape is assumed to be identical to the distribution of the bodies in the primordial belt. Population P48 is reconstructed by taking all bodies brighter than $H_r = 5$ and within 48 au from the MPC database (histograms) while bodies $5 \leq H_r \leq 8.3$ are assumed to follow the completeness-corrected distribution from OSSOS++. The corresponding cumulative mass function is given by the black curve. The conversion between mass and magnitude (top) assumes an albedo typical to hot belt bodies (see Appendix A). The dotted lines labeled $p = -2.0$ and $p = -2.5$ correspond to $N_{<m} \propto m^{1+p}$ with $p = -2$ indicating an equal amount of mass per logarithmically spaced mass bin (the corresponding indices in terms of a radius spectrum $dN/dR \propto R^q$ are $q = -4$ and $q = -5.5$, respectively). Pebble accretion operates to selectively grow the largest TNOs, flattening the size distribution.

The structure of the Paper is as follows. In Section 2, we describe our simplified model to follow the growth of planetary bodies by pebbles. The simplified nature allows exploration by MCMC methods (Section 3). In Section 4, the implications of these findings are reported in the context of solar system formation models. Further assessment of our model is given in Section 5 and the conclusions are given in Section 6.

2. Model

This section consists of three parts. In Section 2.1, we reconstruct a population of TNOs that is complete, against which the model outcome can be evaluated. Section 2.2 describes the pebble accretion model, which is formulated in dimensionless units. While this approach makes the model more abstract, it avoids the need of introducing a specific disk model. Finally, in Section 2.3, we construct the MCMC likelihood function and outline the model parameters.

2.1. The mass function of the dynamical hot population

In Figure 2, we have reconstructed the present-day mass distribution of dynamically hot TNOs within 48 au, a population we refer to as P48. This distribution is composed of two parts. At high masses, we take the bodies directly from the Minor Planet Center (MPC) database³ and filter out the cold classicals by applying an $i_{\text{free}} < 4^\circ$ cut (Huang et al. 2022). Specifically, we assume the data, which includes the entire hot belt, inner belt, 3:2 population (plutinos), 2:1 population (twotinos), as well as scattering TNOs, is complete for $H_r < 5$ bodies within $a \leq 48$ au (Weryk et al. 2016; Petit et al. 2023).

³ The file `distant_extended.dat` was retrieved from <https://www.minorplanetcenter.net/data> on November 9 2024.

We exclude 13 members that belong to the Haumea collisional family, as they are likely fragments ejected from Haumea during/after Neptune’s migration (Proudford & Ragozzine 2019), and are therefore unrelated to the prior pebble accretion process. To account for the lost mass of the Haumea impactor (which could be a moon of Haumea or a dwarf planet from the scattering disk depending on the hypothesis), we include a new body with a mass equal to 3% of Haumea’s (Vilenius et al. 2018; Pike et al. 2020) in our sample. Additionally, we add Neptune’s largest moon, Triton,⁴ which is believed to be a captured moon from the primordial belt (Agnor & Hamilton 2006), as well as Pluto’s largest moon, Charon, which likely formed from a giant impact (Canup 2005). In total, 66 bodies constitute the high-mass portion of the P48 population (see Table A.1), reflecting our current best understanding of the dwarf planet size distribution.

TNOs dimmer than $H_r = 5$ in P48 are modeled on the debiased distribution of the hot belt⁵, based on the OSSOS++ survey (Petit et al. 2023). Their Figure 1 presents the differential distribution, which we fit by a broken power law

$$\Delta \frac{d \log_{10} N}{dH} = \begin{cases} 0.95H_r - 3.45 & (5.0 \leq H_r \leq 6.8) \\ 0.55H_r - 0.73 & (6.8 \leq H_r \leq 8.3) \end{cases} \quad (1)$$

where $\Delta = 0.25$ dex is the bin spacing adopted by Petit et al. (2023). We further estimate that the hot classicals makes up 50% of the dynamical hot bodies in P48, based on population estimates of $H_r < 8.7$ objects: the hot belt contains 20×10^3 objects (Petit et al. 2023), while the inner belt, twotinos, plutinos, and

⁴ This assumes that the implantation probability of bodies ending up as TNOs is similar to the capture probability by Neptune.

⁵ Haumea family members with $H_r > 5$ are not corrected, as the OSSOS survey reveals a significant scarcity of small members within the Haumea family (Pike et al. 2020).

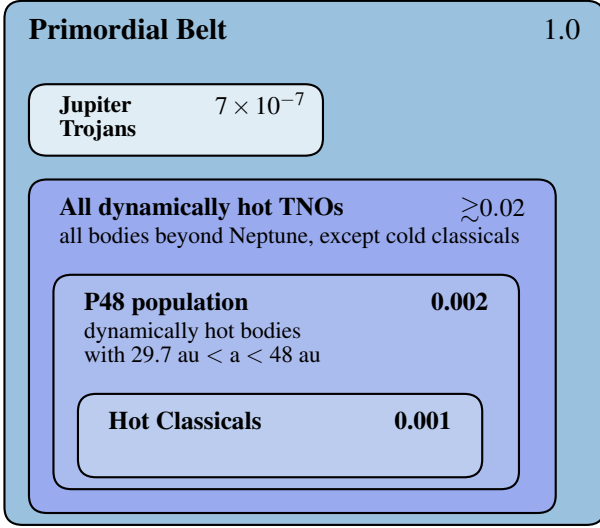


Fig. 3. Implantation fractions for bodies of the primordial belt into the Trojans, hot classicals, and P48. Numbers in bold are used in this work (see text for motivation) and others are given as context. The numbers for the Jupiter Trojans follow Nesvorný et al. (2013) and those for the entire dynamically hot TNO population Nesvorný et al. (2016) and Huang (2023).

scattering populations within $a < 48$ au contain 3, 4.4, 8, and 3×10^3 objects, respectively (Petit et al. 2011; Volk et al. 2016; Chen et al. 2019). The fraction of hot belt TNOs in P48 is thus $20/(20+3+4.4+8+3) \approx 0.5$. Therefore, we multiply the number N that follows from Equation (1) by a factor 2 when reconstructing the P48 distribution (see Figure 3).

In Figure 2, the cumulative distribution of bodies in P48 is plotted alongside the debiased distribution of the cold belt, which is well described by an exponentially tapered power law (Kavelaars et al. 2021). Converted in terms of mass (see Appendix A), the mass function reads:

$$N_{>m} = N_{\text{pre}} \left(\frac{m}{m_{\text{brk}}} \right)^{-\alpha} \exp \left[- \left(\frac{m}{m_{\text{brk}}} \right)^\gamma \right], \quad (2)$$

where for the cold belt $\alpha = 0.67$, $\gamma = 0.42$, and the mass scale indicating the transition to the exponential cut-off regime, $m_{\text{brk}} = 2 \times 10^{20}$ g ($D \approx 70$ km). In Equation (2), N_{pre} is a normalization factor, which, for the specified values of α and γ , can be expressed in terms of the total mass in the belt, m_{belt} , as $N_{\text{pre}} = m_{\text{belt}}/2.81m_{\text{brk}}$. It is important to note that converting between magnitude H_r and mass depends on albedo, which varies between bodies in the hot and cold belts. Consequently, any similarity in the magnitude distributions of the cold and hot belt populations (Petit et al. 2023) does not necessarily imply similarity in the mass distributions. To account for this, we treat m_{brk} as a model parameter. Along with the total initial mass m_{imf} of the primordial belt, this parameter defines the initial distribution prior to pebble accretion.

2.2. Growth of bodies by pebble accretion

Not accounting for gravitational effects, a spherical body of radius R and mass m will sweep up pebbles at a rate $dm/dt = \pi R^2 \rho_{\text{peb}} \Delta v$, where ρ_{peb} is the mass density of pebbles and Δv the approach velocity. Defining $q = m/m_\star$ and $\sigma = \Delta v/v_K$ as the dimensionless mass and relative velocity with $v_K = r\Omega_K$ as the Keplerian velocity corresponding to orbital radius of r , we can

rewrite the accretion rate as

$$\frac{dq}{dt} = A_{\text{geo}} \frac{\chi_\bullet^2 \sigma q^{2/3}}{t_0}, \quad (3)$$

where χ_\bullet is the ratio of the physical-to-Hill radius

$$\chi_\bullet = \frac{R}{r} \left(\frac{3m_\star}{m} \right)^{1/3} = \left(\frac{9m_\star}{4\pi\rho_\bullet r^3} \right)^{1/3} \approx 10^{-4} - 10^{-3}, \quad (4)$$

where ρ_\bullet the internal density of the planetary body and $A_{\text{geo}} = \pi/3^{2/3} \approx 1.5$. Also, the characteristic growth timescale is

$$t_0 = \frac{M_\odot}{\rho_{\text{peb}} r^3 \Omega} \quad (5)$$

$$= 3.5 \times 10^4 \text{ yr} \left(\frac{Z_{\text{peb}}}{0.01} \right)^{-1} \left(\frac{\Sigma_{\text{gas}} r^2 / M_\odot}{0.01} \right)^{-1} \frac{H_{\text{gas}}/r}{0.07} \frac{\Omega^{-1}}{20 \text{ yr}}, \quad (6)$$

where $\rho_{\text{peb}} = Z_{\text{peb}} \rho_{\text{gas}} = Z_{\text{peb}} \Sigma_{\text{gas}} / \sqrt{2\pi} H_{\text{gas}}$ the mass density of pebbles in the midplane, Z_{peb} the corresponding local ‘‘metallicity’’, Σ_{gas} the surface density of the gas and H_{gas} the gas pressure scaleheight. The disk aspect ratio $h = H_{\text{gas}}/r$ can also be written

$$h = \sqrt{\frac{k_B T r}{\mu m_u G m_\odot}} = 0.069 \left(\frac{T}{60 \text{ K}} \right)^{1/2} \left(\frac{r}{20 \text{ au}} \right)^{1/2}, \quad (7)$$

where T is the temperature in the midplane and $\mu = 2.34m_u$ the mean molecular weight of the gas.

The degree of coupling between particles and gas is quantified by the particles’ stopping time t_{stop} , which represents the time for a particles to adjust its motion to that of gas. Its dimensionless equivalent, $\tau_s = \Omega_K t_{\text{stop}}$, is referred to as the aerodynamic size (in the literature, ‘‘Stokes number’’ or St is also common). In this work, we define pebbles as particles of $\tau_s < 1$. For Epstein drag, τ_s can be expressed as $\tau_s = \pi(\rho_\bullet R)_{\text{peb}} / 2\Sigma_{\text{gas}}$, indicating that aerodynamic size is proportional to R_{peb} .

The relative velocity $\Delta v = \sigma v_K$ can be identified with either:

- The eccentricity of planetesimals, $\Delta v \approx e v_K$ ($\sigma = e$). This is not considered in this work.
- The headwind velocity of the gas. Due to the radial pressure gradient, the azimuthal motion of the gas lags the Keplerian motion by an amount $\Delta v = \eta v_K$ ($\sigma = \eta$), where

$$\eta \equiv - \frac{1}{2} \frac{\partial \log P}{\partial \log r} h^2 = 4.9 \times 10^{-3} \left(\frac{\partial_{\log r} \log P}{-2} \right) \left(\frac{h}{0.07} \right)^2 \quad (8)$$

(e.g., Weidenschilling 1977) is a parameterization of the radial pressure gradient. Pebbles with $\tau_s < 1$ follow the gas, while planetesimals ($\tau_s \gg 1$) move at the Keplerian velocity. Hence, the pebble-planetesimal velocity is also ηv_K .

- The turbulent velocity $\Delta v \approx \mathcal{M} c_s$ ($\sigma = \mathcal{M} h$), where \mathcal{M} is the Mach number of the turbulent flow and h is the disk aspect ratio.

Crudely, the largest of these velocities – e , η , or $\mathcal{M} h$ – determines Δv .

Gravitational focusing increases the accretion rate by a factor $(v_{\text{esc}}/\Delta v)^2 = 2Gm/R(\Delta v)^2$, where v_{esc} is the escape velocity from its surface. In dimensionless units, the rate becomes

$$\frac{dq}{dt} = A_{\text{saf}} \frac{\chi q^{4/3}}{(\sigma + q^{1/3}) T}, \quad (9)$$

with $A_{\text{Saf}} = 2\pi/3^{1/3} \approx 4.4$. Here, we add a term $q^{1/3}$ in the denominator in order to account for the Keplerian shear component of the relative velocity, which becomes important when σ is low.

Gravitational focusing significantly enhances the growth rates of planetesimals. On the other hand, its efficacy is hampered by the more copious non-collisional scatterings of planetesimals – a process known as viscous stirring (Ida & Makino 1993) – or turbulent stirring (Ida et al. 2008), which increases Δv . For small pebbles tightly coupled to the gas, this is not a concern, because gas drag circularizes their orbits before the next encounter. Therefore, in contrast to planetesimals, there is no need to follow the evolution of Δv with time.

More potently, pebbles are accreting by the settling mechanism – better known as pebble accretion (Ormel & Klahr 2010; Lambrechts & Johansen 2012). In pebble accretion, pebbles can be captured at distances much larger than R , whereafter the pebbles settle down in the gravitational potential. We adopt the numerically-calibrated expression by Ormel & Liu (2018)⁶:

$$\frac{dq}{dt} = A_{\text{peb}} \frac{q\tau_s}{t_0} f_{\text{set}}^2, \quad (10)$$

with $A_{\text{peb}} = 12.3$ and $f_{\text{set}} \leq 1$ being a modulation factor that suppresses accretion rates at small masses. It is a defining characteristic of pebble accretion that rates do not depend on the physical radius (or the nondimensional χ_* parameter; Ormel 2017). In addition, we have assumed the 3D accretion regime for pebbles in Equation (10), for which σ does not enter explicitly. The velocity matters in the modulation factor f_{set} , however:

$$f_{\text{set}}^2 = \exp\left[-\left(\frac{\Delta v}{v_*}\right)^2\right] \quad \text{or} \quad f_{\text{set}}^2 = \left[1 + a_{\text{turb}} \left(\frac{\Delta v}{v_*}\right)^2\right]^{-3}, \quad (11)$$

with $v_* = (q_p/\tau_s)^{1/3} v_K$ and $a_{\text{turb}} = 0.33$ (Liu & Ormel 2018). The first expression in Equation (11) holds for a laminar-dominated velocity field and the second for a turbulent-dominated Δv . In the case of a turbulent flow, Δv should be regarded as the rms value of an underlying velocity distribution that is isotropic (Ormel & Liu 2018).

Figure 4 presents the Safronov and settling growth rates as functions of mass. Here, the rates are expressed in terms of the growth timescale, $t_{\text{gr}} = m/(dq/dt)$, which is given in units of t_0 (see Equation 5). At low masses, accretion is dominated by gravitational focusing (Safronov limit; yellow curve). It is well-known that in this limit, the growth timescale decreases with the mass: the runaway growth regime (Wetherill & Stewart 1989). Pebble accretion (the settling mechanism) is unimportant at low masses. Yet at a mass scale that is a fraction of $q_* = \sigma^3 \tau_s$ (the mass corresponding to $\sigma \sim v_*$), the settling mechanism starts to become efficient, increasing the growth rate significantly (Visser & Ormel 2016). In the case of a turbulence-dominant velocity field, this transition is slightly less abrupt (thin line). Hence, bodies more massive than $\sim 0.1 m_*$ will undergo rapid growth, while those with $m \ll m_*$ grow more slowly. Pebble accretion therefore has the potential to flatten the high-mass tail of the size distribution, illustrated in Figure 4 by the gray arrows.

2.3. Model parameters and likelihood

An overview of the parameters in the model is given in Table 1. The initial distribution of bodies is specified by parameters m_{brk}

⁶ Ormel & Liu (2018) express these expression in terms of an efficiency $\epsilon = \dot{M}/2\pi r \Sigma v_r$. We take their 3D expression, $\epsilon = 0.39q/\eta h_{\text{peb}} \times f_{\text{set}}^2$. With the drift velocity $v_r = 2\eta v_K \tau_s$ and $\rho_{\text{peb}} = \Sigma_{\text{peb}}/\sqrt{2\pi} h_{\text{peb}}$, we obtain Equation (10).

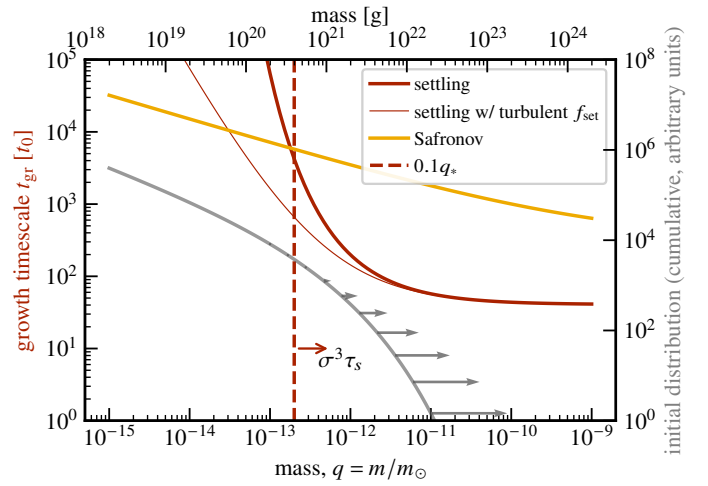


Fig. 4. Growth timescales for pebble accretion (settling mechanism, red) and Safronov accretion (gravitational focusing in the absence of gas drag; yellow) for a velocity parameter of $\sigma = \Delta v/v_K = 10^{-3}$, dimensionless stopping time $\tau_s = 2 \times 10^{-3}$, and internal density parameter $\chi_* = 5 \times 10^{-4}$. The critical mass $q_* = \sigma^3 \tau_s$ (or rather a fraction of this number; vertical dashed line) indicates the point where the settling mechanism becomes operational. In the case where the approach velocity is due to turbulence, such that Δv follows a distribution, the transition is more gradual (thin red line). Pebble accretion acts on the high-mass tail of the distribution where the length of the arrows is proportional to the growth rate (Equation (10); gray).

and the initial mass of the belt m_{imf} (see Equation 2), which are uniformly sampled in the log space. Pebble properties are given by their dimensionless velocity σ , the dimensionless stopping time τ_s , and the total accreted pebbles mass m_{peb} . In addition to the continuous sampling of these parameters, the model also employs a binary switch for the nature of the velocity field laminar or turbulent. If the velocity is laminar, σ is identified with the normalized pressure gradient parameter η ; if turbulent, with the Mach number of the turbulent velocity field. The velocity field matters in calculating the f_{set} modulation factors (see Equation 11).

In total, the sampling provides us with several hundreds bodies, which covers the entire mass distribution. The mass of each of the bodies is integrated over time. We work in dimensionless units where time is normalized by t_0 (Equation 5) and mass by the mass of the Sun. The pebble accretion rate dq/dt is computed for each of these bodies, according to the collision rates given in Section 2.2. The bodies do not interact among themselves; and because dq/dt is an increasing function of q , the initial order of their masses stays preserved. Under these conditions, the calculation boils down to a set of ordinary differential equations, which we solve with the `scipy.integrate.odeint` library. Simultaneously with the increase of q , we decrease the mass of the pebble reservoir q_{peb} , whose initial value is also a parameter. When q_{peb} reaches 0, we stop the simulation and record the elapsed time t (in units of t_0). This distribution is then weighted by the implantation factor f_{impl} , the ratio between numbers of bodies in the present-day P48 and in the primordial belt, to obtain the simulated distribution of bodies in P48.

The likelihood function is calculated by comparing the simulated distribution with the reconstructed distribution in the OS-SOS++ domain and the observed number of bodies in the MPC domain (see Figure 2). To this effect, the particles are binned by mass, with 10 bins covering the OSSOS++ region and 15 covering the MPC region (the bin width is about 0.2 dex). The

Table 1. Model parameters.

Description	Symbol	Unit	Value/Range	Reference/comment
second component mass fraction	f_2		$\mathcal{U}(0, 0.3)$	only in model featuring a second particle size
mass in accreted pebbles	m_{peb}	$[m_{\oplus}]$	$\mathcal{L}(1, 10^3)$	includes only the mass of pebbles that are consumed
primordial belt characteristic mass	m_{brk}	[g]	$\mathcal{L}(2 \times 10^{19}, 2 \times 10^{22})$	
mass in primordial belt (planetesimals)	m_{imf}	$[m_{\oplus}]$	$\mathcal{L}(0.3, 105)$	
pebble aerodynamic size (Stokes number)	τ_s		$\mathcal{L}(10^{-4}, 1)$	
second pebble aerodynamic size	τ_2		$\mathcal{L}(10^{-4}, 1)$	only in model featuring a second particle size
pebble relative velocity	$\sigma = \Delta v/v_K$		$\mathcal{L}(4 \times 10^{-5}, 0.1)$	relative velocity between bodies and pebbles
– headwind parameter	$\sigma = \eta$			see Equation (8)
– turbulent Mach number	$\sigma = \mathcal{M}h$			Δv follows a distribution; h is the aspect ratio of the disk and \mathcal{M} the turbulence Mach number.
internal density parameter	χ		5×10^{-4}	Equation (4). Irrelevant for pebble accretion.
implantation factor	f_{impl}		2×10^{-3}	fraction of bodies in the primordial belt that ends up in P48.

Table 2. List of model runs and posterior values for the MCMC simulations.

model	$\log_{10} \sigma$	$\log_{10} \tau_s$	$\log_{10} \tau_2$	f_2	$m_{\text{brk}} [10^{20} \text{ g}]$	$m_{\text{imf}} [m_{\oplus}]$	$m_{\text{peb}} [m_{\oplus}]$	$C_{\tau\sigma}$	$\ln \mathcal{P}$
lami-1p	$-2.78^{+0.40}_{-0.38}$	$-1.70^{+1.15}_{-1.22}$			$8.90^{+2.12}_{-1.96}$	$11.61^{+1.00}_{-1.08}$	$5.22^{+4.09}_{-2.25}$	$-10.05^{+0.11}_{-0.12}$	-86.64
turb-1p	$-2.56^{+0.41}_{-0.49}$	$-2.12^{+1.46}_{-1.27}$			$6.69^{+1.96}_{-1.49}$	$11.39^{+1.24}_{-2.12}$	$7.60^{+5.45}_{-3.61}$	$-9.81^{+0.13}_{-0.13}$	-86.14
lami-2p	$-2.92^{+0.43}_{-0.30}$	$-1.88^{+1.27}_{-1.36}$	$-1.96^{+1.32}_{-1.33}$	$0.14^{+0.11}_{-0.10}$	$8.14^{+2.20}_{-2.36}$	$11.61^{+1.02}_{-1.09}$	$5.60^{+4.48}_{-2.47}$	$-10.12^{+0.15}_{-1.74}$	-86.10
turb-2p	$-2.84^{+0.52}_{-0.30}$	$-1.88^{+1.32}_{-1.48}$	$-2.30^{+1.58}_{-1.19}$	$0.15^{+0.10}_{-0.10}$	$6.21^{+1.86}_{-1.57}$	$11.66^{+1.14}_{-1.34}$	$7.10^{+5.30}_{-3.28}$	$-9.86^{+0.16}_{-0.62}$	-85.96

Notes. See Table 1 for the parameters and Equation (15) for $C_{\tau\sigma}$. The lower and upper values indicate the 16% and 84% posterior ranges. The last column gives the maximum likelihood of the sample.

number of bodies in the synthetic and observed distributions are then compared for each bin. In the OSSOS++ region, Gaussian statistics are assumed, i.e., the contribution to the log-likelihood of bin k equals:

$$\ln \mathcal{P}_k^{\text{OSSOS++}} = -\frac{1}{2} \left(\frac{N_k - N_{\text{sim},k}}{\sigma_k} \right)^2 - \frac{1}{2} \ln(2\pi\sigma_k^2) \quad (12)$$

where $N_{\text{sim},k}$ is the simulated number of bodies, N_k is the observed number of bodies in P48, as obtained from Equation (1), and σ_k represents the spread. The spread σ_k is also obtained from the debiased OSSOS++ distribution⁷. For the MPC part, we use binomial statistics to obtain the likelihood contribution:

$$\ln \mathcal{P}_k^{\text{MPC}} = \ln \mathcal{B}(N_k, N_{\text{sim},k}, f_{\text{impl}}) \quad (13)$$

where $\mathcal{B}(x, n, p)$ is the probability of drawing x successes out of n independent samples where each draw has probability p .

In addition, we apply two priors to the likelihood function, related to the following observations:

- The number of Jupiter Trojans constrain the total mass of the primordial belt $m_{\text{imf}} + m_{\text{peb}}$. Since the Jovian Trojans are also thought to be captured from the same disk, the mass of bodies present in the primordial belt can be estimated using a numerically simulated implantation rate and the observed mass of the Trojans (see Figure 3 and Nesvorný et al. 2013). The total pre-instability mass of the primordial belt falls in the range of 14–28 m_{\oplus} . Consequently, we add a term \mathcal{P}^{PB} to the likelihood function corresponding to a situation where the parameter $\mu = \ln(m_{\text{imf}} + m_{\text{peb}})$ is normally distributed, centered around $\ln 20 m_{\oplus}$ and with spread $\sigma = 0.34$.

- The preservation of the dynamically cold classicals, limits the mass of individual bodies. If any planetary-mass bodies formed in the primordial outer disk and were scattered out by a migrating Neptune, the cold classical belt will likely be overheated or even destroyed by the gravitational sweeping of such a planet. Therefore, the masses of the individual bodies making up the primordial belt could not have been too large. Petit et al. (1999) simulated the effect of massive protoplanets on the stability of the cold belt, and found a threshold mass of $\sim 1 m_{\oplus}$. To incorporate this mass constraint, we add a term $\ln \mathcal{P}^{\text{CC}} = -(m_1/m_{\oplus})^2$ to the log-likelihood function, which suppresses models favoring formation of bodies beyond 1 Earth mass.

The total log-likelihood is then

$$\ln \mathcal{P} = \sum_k \ln \mathcal{P}_k^{\text{MPC}} + \sum_k \ln \mathcal{P}_k^{\text{PB}} + \ln \mathcal{P}^{\text{CC}} + \ln \mathcal{P}^{\text{PB}} \quad (14)$$

We then conduct an MCMC analysis using *emcee* (Foreman-Mackey et al. 2013), marginalizing over the input parameters listed in Table 1.

3. Results

The posterior values of the model parameters from the MCMC fit are summarized in Table 2. Four model suites are considered, each characterized by binary choices for the velocity field—either laminar (lami-) or turbulent (turb-)—and the particle components—a single particle size (1p) or two pebble sizes (2p). Models with two particle sizes feature two additional parameters: the aerodynamic size (τ_2) and the mass fraction of the second component (f_2).

⁷ We estimate the 2σ error, again from inspecting Figure 1 of (Petit et al. 2023), to be decreasing linearly with H_r from 0.4 dex at $H_r = 5$ to 0.13 dex at $H_r = 6.8$, whereafter it stays constant at this value.

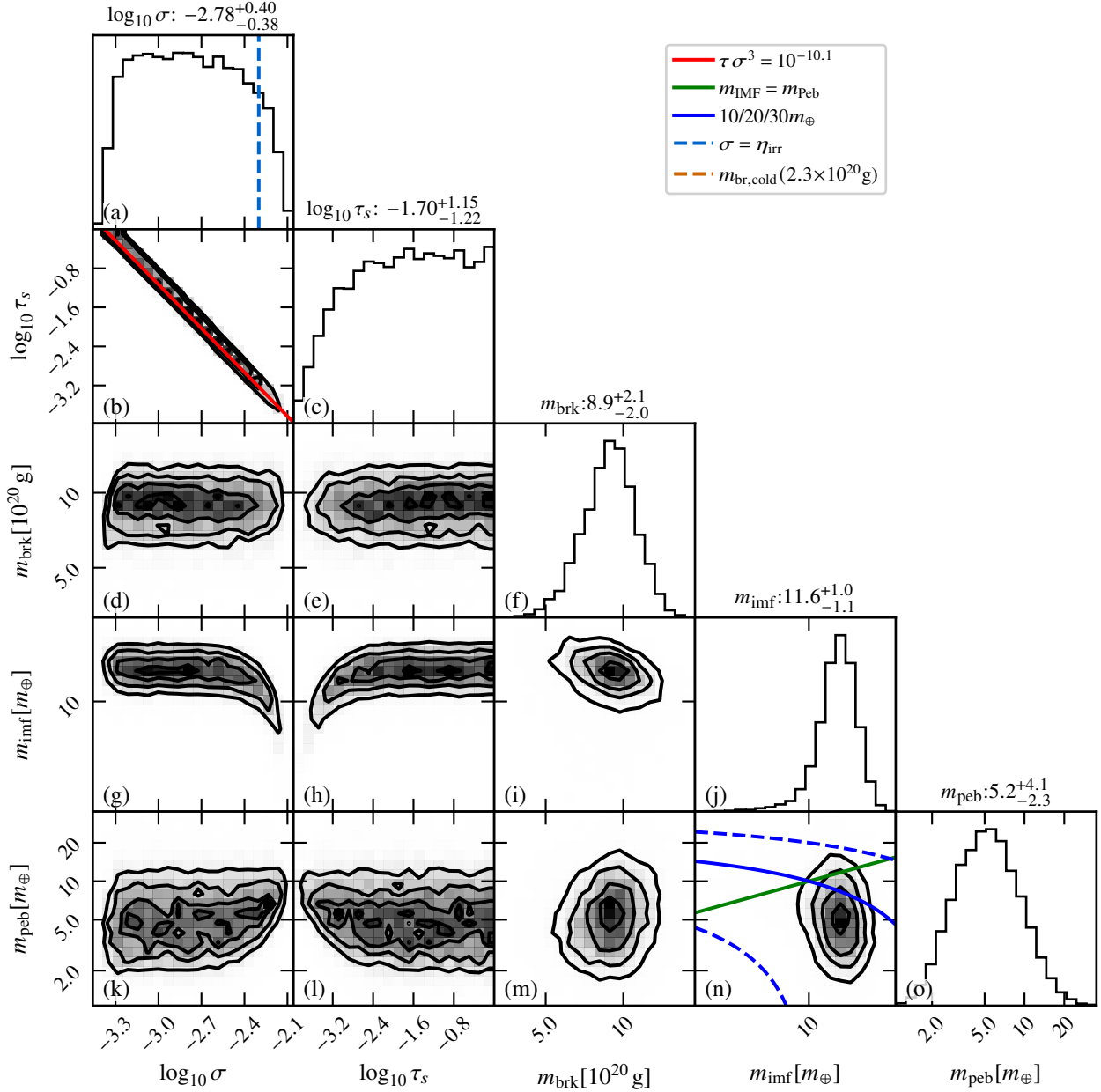


Fig. 5. MCMC posterior distribution of the single particle laminar model (1ami-1p). The 16%, 50%, and 84% confidence levels are indicated above each histogram. Runs cluster around the line of constant $\tau_s \sigma^3$, which indicates a mass scale above which pebble accretion operates (panel b). High-velocity solutions, like in a smooth disk ($\sigma = \eta_{\text{irr}}$), have difficulty fitting the data (panel a). The amount of accreted pebbles is lower than the mass of the initial population by around 0.4 dex (panel n).

3.1. Simulations with a single particle component

Figure 5 presents the corner plot of the 1ami-1p model (laminar velocity field with one pebble size). The most striking feature is the correlation between the stopping time τ_s and the relative velocity (see panel b). The slope of this correlation is -3 , which points to a mass scale where pebble accretion is initiated, $q_* = \sigma^3 \tau_s$. Specifically, we fit

$$C_{\tau\sigma} \equiv \log_{10} \tau_s \sigma^3 = \log_{10} \tau_s + 3 \log_{10} \left(\frac{\Delta v}{v_K} \right) = -10.05^{+0.11}_{-0.12}. \quad (15)$$

In physical units, $m_* = 10^{C_{\tau\sigma}} m_\odot \approx 1.6 \times 10^{23} \text{ g}$ (or $10^{-5} m_\oplus$); the actual mass where pebble accretion starts to dominate over Safronov accretion is $\approx 10\%$ of this number; see Figure 4). For bodies of mass $m > m_*$, pebble accretion is fully operational,

whereas below m_* pebble accretion is suppressed. Therefore, for $m \ll m_*$, the mass distribution tends to follow the IMF, as given by the m_{brk} and m_{imf} parameters. However, due to the exponential tapering at high mass, the IMF cannot fit the high-mass end of the P48 bodies. Here, pebble accretion acts to flatten the mass distribution (see Figure 4). Table 2 shows that about 5–8 Earth mass in pebbles are needed—an amount that is similar to the mass in the IMF.

At high velocity, the correlation starts to break down. Here, the combination of high σ and small τ_s renders pebble accretion very slow (Equation (10)) and allows ballistic encounters (Safronov focusing) to rival pebble accretion. As a result, the mass distribution at low mass is altered, which is demonstrated by the 1ami-1p-etairr model, which features a σ value consistent with that of an irradiated disk. Figure 7 illustrates that

Table 3. Parameters of several runs presented in Figure 6.

name	σ	τ_s	τ_2	f_2	m_{brk} [10^{20} g]	m_{inf} [m_{\oplus}]	m_{peb} [m_{\oplus}]	mode	time [t_0]	$\Delta \ln \mathcal{P}$
lami-1p-best	1.1×10^{-3}	0.074			8.7	12	7.8	L	9.1	0.0
lami-1p-etairr	6.4×10^{-3}	3.4×10^{-4}			10	10	8.4	L	1.8×10^3	-1.2
lami-1p-himass	1.1×10^{-3}	0.092			11	11	11	L	7.6	-1.1
turb-1p-best	9.7×10^{-3}	1.4×10^{-4}			10	6.1	12	T	4.6×10^3	0.50
turb-1p-hitau	1.1×10^{-3}	0.16			8.1	11	13	T	5.5	-0.68
lami-2p-best	5.1×10^{-3}	4.0×10^{-4}	5.2×10^{-3}	0.085	7.4	10	8.3	L	1.2×10^3	0.54
turb-2p-best	8.6×10^{-3}	1.8×10^{-4}	1.9×10^{-4}	0.25	7.2	7.6	11	T	3.8×10^3	0.68

Notes. The last two columns denote the time (in units of t_0) to complete the run and the change in log-likelihood with respect to the lami-1p-best model.

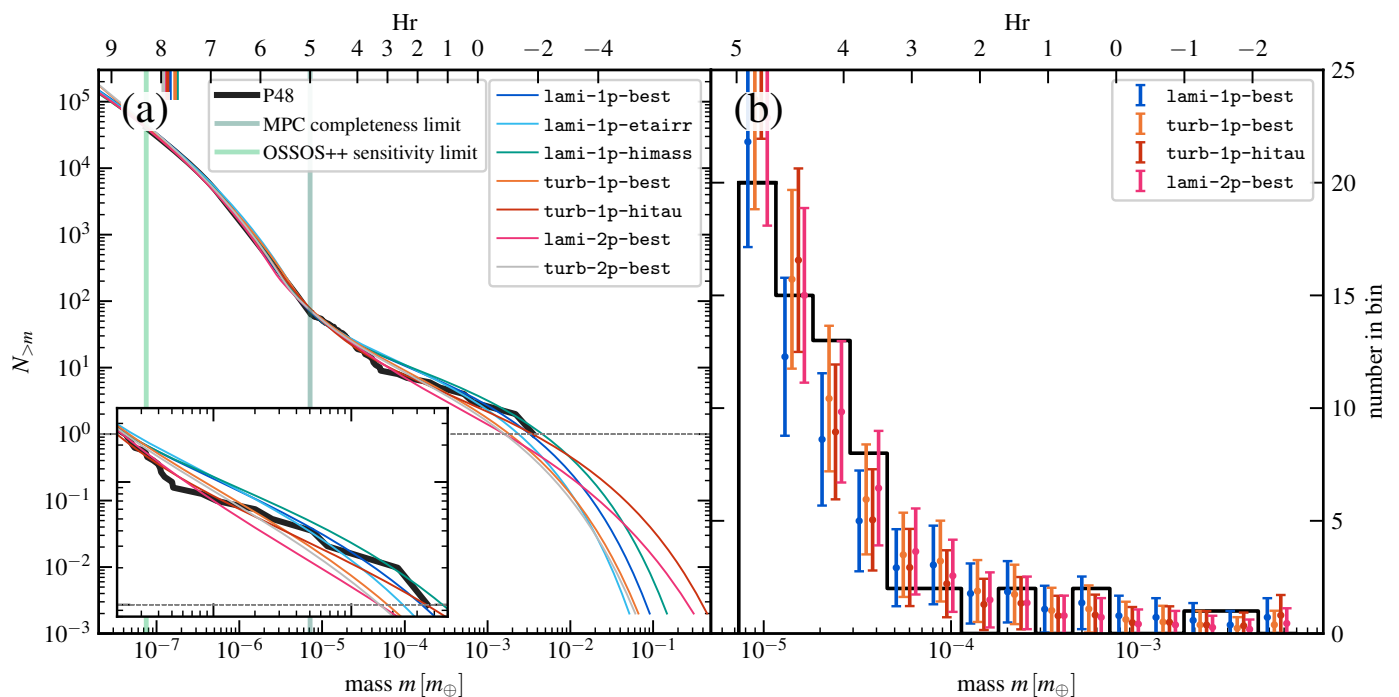


Fig. 6. Cumulative distributions (a) and histograms (b) of sample model runs. An implantation factor of $f_{\text{impl}} = 2 \times 10^{-3}$ has been applied, after which the simulated distributions can be compared to the P48 population (black). In (b) the low number of bodies (and large Poisson error bars) illustrate why the fits tend to be rather insensitive to the specifics at the high-mass end of the distribution. Runs featuring small τ_s are associated with high σ due to the degeneracy between these quantities (see Table 3). Runs with small τ_s are disfavored, however, as pebble accretion operates too slowly.

in this model low-mass bodies accrete a significant amount of pebbles. As σ increases, this trend becomes more pronounced resulting in poorer fits, because the OSSOS++ part of the distribution can no longer be matched. This finding is unsurprising as the shape of the IMF was adopted from the cold classicals, which was already shown to fit the shape of hot classicals across the OSSOS++ range (Kavelaars et al. 2021; Petit et al. 2023). But it also shows that accretion processes cannot maintain the shape of the low-mass part—at least not in conjunction with also matching the high-mass tail. It further lends support to the primordial nature of the low-mass part of the TNO size distribution.

An additional concern for these small τ_s runs is that they take a long time (t/t_0 is high). We can estimate the characteristic accretion time for pebble accretion from the pebble accretion rate (Equation (10)): $t \sim q/\dot{q} \sim t_0/\tau_s$, for $f_{\text{set}} \sim 1$ (i.e., $m > m_*$). This estimate agrees with Table 3 where we compiled t/t_0 for selected model runs. Recall that the simulations are conducted

in dimensionless parameter space, where we can hide our ignorance of, e.g., the pebble density, which sets the value of t_0 (Equation 5). Yet, the pebble accretion mechanism requires gas-rich conditions and it must terminate *before* the lifetime of the gas-rich disk, typically estimated at ~ 5 Myr (Weiss et al. 2021). Therefore, a high t/t_0 renders these models implausible. We return to the timescale constraints in Section 4.

Table 2 shows that a turbulent velocity field marginally improves the log-likelihood of the best model by an amount of +0.5. This specific run is characterized by a very low τ_s value (turb-1p-best entry in Table 3), which is disfavored in the light of above discussion. A higher τ_s run, following the τ_s - σ correlation (turb-1p-hitau) fits the data equally well. Figure 6a presents cumulative distribution of several individual runs. All models overshoot the inflection point at $m = 10^{-4} m_{\oplus}$ and also tend to undershoot the final bin where the observed CMF terminates (with Triton) at $m = 3 \times 10^{-3} m_{\oplus}$. These appar-

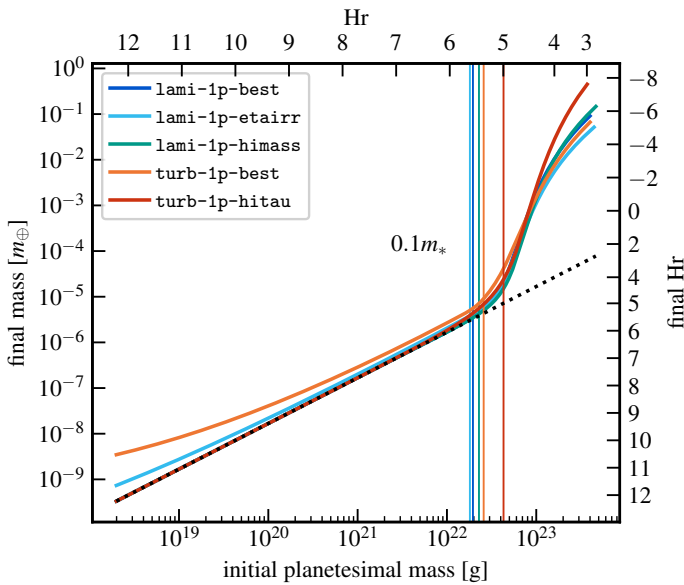


Fig. 7. Final vs initial mass for several simulation runs (see Table 3). Vertical lines denote 10% of $m_* = \sigma^3 \tau_s m_\odot$, which is the scale where pebble accretion kicks in. Dashed line is the identity line ($y = x$). Bodies $\geq 10^{22}$ grow their mass by pebble accretion many tenfolds and become dwarf planets. The gain in mass at low mass in the lami-1p-etairr and turb-1p-best is due to the slow pace of pebble accretion, allowing Safronov interactions to become important at low planetesimal mass.

ent mismatches are a consequence to the low number of TNOs at these masses, which can be understood from inspecting the differential distribution (on which the likelihood calculations are based). Figure 6b presents these fits for the MPC part of the distribution. Here, the error bars denote Poisson counting uncertainties. The bin to the right of $m = 10^{-4} m_\oplus$ with 0 bodies in the MPC is typically fitted with ≈ 2 bodies in the simulation, but this still has a Poisson likelihood of 13.5%. Similarly, the simulation runs are quite insensitive to the presence of the two most massive bodies (Pluto and Triton); statistically, the low number of high- m bodies do not carry much weight. As a result the runs that under-shoot the cumulative curve in Figure 6a (e.g., turb-1p-best) statistically cannot be distinguished from those runs that include a larger τ_s (e.g., turb-1p-hitau) and those runs that contain more pebbles (e.g., turb-1p-himass).

3.2. A second particle component

Addition of a secondary component does not significantly improve the results. From Table 2, the Bayes factor (the difference in $\ln \mathcal{P}$) is 0.54 between the laminar models and 0.18 between the turbulence models. These values indicate that the added parameters have insignificant effects on the fits (Jeffreys 1998). This insensitivity is reflected in Table 2 by the proximity of the size of the secondary component (τ_2) to that of the main component (τ_s) in the lami-2p and turb-2p models. Figure 6 presents this result graphically. The lami-2p-best run—the run where \mathcal{P} is the highest—hardly stands out from the other runs. Curiously, these models tend to be fitted by low τ_s (and τ_2) and correspondingly high t_0 , indicating these runs improve the fit for the OS-SOS++ part of the distribution, rather than the high-mass MPC part. In other words, the low number of high-mass bodies in P48 prevents any meaningful fit for the high-mass end of the distri-

bution, which makes the model insensitive to a second particle component.

While we do not find evidence for a binary distribution of pebbles, two points should be noted. First, the size distribution could still be a power-law, which would ameliorate the f_{set} transition in a similar way as the turbulence velocity field would do (Lyra et al. 2023). Second, the lack of evidence for a second component does not preclude its presence. A bigger sample of high-mass bodies is necessary to establish or discount its existence.

4. Implications

The MCMC calculations in the previous section demonstrate that both turbulent and laminar models fit the data. Here, we identify the laminar model with formation in a standard smooth disk, characterized by a spatially constant radial pressure parameter η (Equation (8)). Conversely, the turbulent model corresponds to formation within an environment where pebbles collect around a radial pressure maximum ($\eta \approx 0$) such that velocities are dominated by turbulent motions. This can be identified with pebble rings seen in ALMA.

4.1. Formation in a pebble ring

Pebble rings are ubiquitous in ALMA imagery (Andrews et al. 2018; Bae et al. 2023). Containment of particles by pressure maxima is the leading explanation for the observed particles accumulation in these rings. Around the pressure maximum location $\eta \approx 0$ and the relative motion between pebbles and bigger bodies is due to turbulence. Studies have used the extent of rings in both the vertical and radial dimensions to constrain the diffusivity—the “turbulent alpha”—of the gas. Specifically, this constrains the ratio of gas diffusivity over Stokes number of the particles, α_D/τ_s . Rosotti (2023) compiled results from a number of works that measure the radial width of continuum rings (their Table 2), finding that the inferred α_D/τ_s ranged from a low of 0.04 to values exceeding unity (the latter essentially implies particles follow the pressure distribution). However, α_D/τ_s obtained from the vertical extent of the dust layer are often inferred to be smaller, e.g., $\alpha_D/\tau_s \approx 10^{-2}$ (Villenave et al. 2022). For simplicity, we adopt in the following a range in α_D/τ_s between 0.01 and 0.4, which covers most of these measurements.

When we convert the diffusivity parameter α_D to a root-mean-square (rms) particle velocity, we obtain⁸

$$\frac{\sigma^2}{\tau_s} = \frac{3h^2}{2} \left(\frac{\alpha_D}{\tau_s} \right)_{\text{ALMA}} \approx 7 \times 10^{-4} \left(\frac{h}{0.07} \right)^2 \left(\frac{\alpha_D/\tau_s}{0.1} \right)_{\text{ALMA}} \quad (16)$$

where $(\alpha_D/\tau_s)_{\text{ALMA}}$ is inferred from the extent of the ring in ALMA imagery, and $h = 0.07$ is our adopted value for the aspect ratio of the gas at the location of the primordial belt.

A further constraint to particle sizes in rings comes from the fragmentation barrier (Güttler et al. 2010; Birnstiel et al. 2011). When the gas is turbulent, the pebble-pebble relative velocity

⁸ Here we have related the parameter α_D , which expresses the diffusivity of the gas, to the rms velocity of the turbulent gas motions σ . The turbulent diffusivity of the gas is parameterized in terms of α as in $D_{\text{gas}} = \alpha_D c_s^2 / \Omega$. In general, we can write $D_{\text{gas}} = V_L^2 t_L$ where V_L and t_L are, respectively, the velocities and turnover times of the largest eddies in the turbulent cascade. A common choice for rotating systems is $t_L = \Omega_K^{-1}$ and therefore $V_L = \sqrt{\alpha_D c_s}$ (Cuzzi et al. 2001). Furthermore, if turbulence is Kolmogorov, the rms velocities of the turbulent gas is $\Delta v = \mathcal{M} c_s = (3/2)V_L$. Then, we obtain $\alpha_D = (2\mathcal{M}/3)^2 = (2\sigma/3h)^2$.

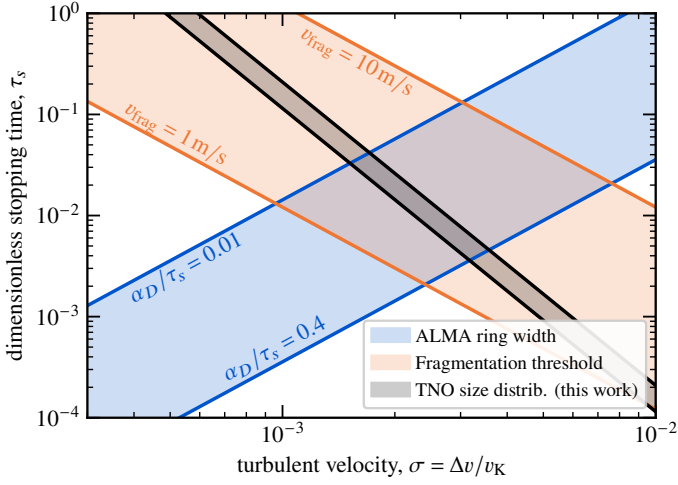


Fig. 8. Constraints on the particle aerodynamic size (Stokes number τ_s) and turbulence intensity of the gas, where σ is identified as the root-mean-square turbulent gas velocity. Constraints follow from simulating the TNO size distribution (run `turb-1p`, black line), ALMA ring morphological analysis (blue lines; Rosotti 2023), and particle fragmentation velocity (orange lines; the adopted value for the Keplerian velocity v_K is the circular motion at 20 au). Under the assumption that the primordial belt featured conditions similar to ALMA rings the degeneracy between τ_s and σ (or α_D ; Equation (16)) can be lifted and we find, $\tau_s \sim 0.01$, $\alpha_D \sim 10^{-3}$, and a fragmentation threshold of $\sim 2 \text{ m s}^{-1}$.

increases with the size (Stokes number) as in $\Delta v_{pp} \approx \mathcal{M}c_s \sqrt{2\tau_s}$ (Ormel & Cuzzi 2007),⁹ where \mathcal{M} is the Mach number of the turbulent flow. The aerodynamic size is then determined by the condition $\Delta v_{pp} = v_{\text{frag}}$, resulting in:

$$\sigma \tau_s^{1/2} = \frac{\mathcal{M}c_s \tau_s^{1/2}}{v_K} = \frac{\Delta v_{pp}}{2^{1/2}v_K} \lesssim 1.1 \times 10^{-4} \left(\frac{v_{\text{frag}}}{1 \text{ m s}^{-1}} \right). \quad (17)$$

These constraints are presented in Figure 8, together with the constraint on $\tau_s \sigma^3$ that we obtained from modelling the TNO size distribution (Table 2). The constraint on the extent of ALMA rings are almost orthogonal to the constraint from the TNO size distribution modelling (this study), allowing us to put meaningful constraints on τ_s and α_D . Together, they point to an aerodynamic size in the range of $\tau_s \sim [3 \times 10^{-3} - 4 \times 10^{-2}]$, a turbulent diffusivity of $\alpha_D \sim [4 \times 10^{-4} - 2 \times 10^{-3}]$, and a fragmentation threshold of $v_{\text{frag}} \sim [1.7 - 3.2 \text{ m s}^{-1}]$.

These values are similar to what was found by Jiang et al. (2024) in a recent analysis, who assumed a fragmentation threshold of $v_{\text{frag}} \sim 1 \text{ m s}^{-1}$. Our results independently suggest that the particle fragmentation threshold amount is $\sim 2 \text{ m s}^{-1}$ in order for particles to grow to the inferred aerodynamic sizes. (A higher fragmentation threshold is possible if the growth of particles is limited by, e.g., bouncing; Zsom et al. 2010.) A fragmentation velocity increase by a factor of 2 would increase the derived value of the fragmentation α in Jiang et al. (2024) by a factor of 4 to $\sim 4 \times 10^{-4}$, in line with our findings.

If the TNO population formed from a ring in which the pebbles are contained by pressure, it is natural to assume that the birth ring would have had a mass in pebbles similar to the accreted pebble mass $m_{\text{peb}} \sim 10m_{\oplus}$. This allows us to constrain the characteristic timescale t_0 , Equation (5). Since $\rho_{\text{peb}} \sim$

$m_{\text{ring}}/2\pi r W_r H_r$, where W_r and H_r are the width and height of the ring, we obtain

$$t_0 \sim 4 \times 10^3 \text{ yr} \left(\frac{m_{\text{ring}}}{10m_{\oplus}} \right)^{-1} \frac{W_r/r}{0.1} \frac{H_r/r}{0.01} \frac{\Omega^{-1}}{20 \text{ yr}}. \quad (18)$$

If the pebble aerodynamic size is $\tau_s \sim 10^{-2}$, it would take a time $\sim t_0/\tau_s$ for these bodies to accrete the pebbles, i.e., $\sim 0.4 \text{ Myr}$, for the geometrical factors W_r/r and H_r/r adopted above. This time falls within the typical lifetimes of the solar nebula disk (Weiss et al. 2021), implying that pebbles will be consumed before the disk dissipates. However, very wide rings ($W_r/r \sim 1$ or $H_r/r \sim 0.1$) would dilute the concentration of pebbles and render pebble accretion much slower.

4.2. A laminar disk

If pebbles are not entrained by a pressure maximum and freely drift inward, the relative velocity between planetesimals and pebbles is given by the global disk pressure gradient η . From Equation (8), $\sigma = \eta \approx 5 \times 10^{-3}$ for a power-law index of pressure on radius of 2 and from the τ_s - σ relationship (Equation (15)), we then find an aerodynamic size of a mere $\tau_s = 7 \times 10^{-4}$, which is rather small for pebbles. Indeed, the radial drift timescale

$$t_{\text{drift}} = \frac{r}{v_r} = \frac{1}{2\eta\tau_s\Omega} \quad (19)$$

$$= 2 \times 10^6 \text{ yr} \left(\frac{\eta}{5 \times 10^{-3}} \right)^{-1} \left(\frac{\tau_s}{7 \times 10^{-4}} \right)^{-1} \left(\frac{r}{20 \text{ au}} \right)^{3/2} \quad (20)$$

already rivals the disk lifetime, suggesting that particles hardly drift. In addition, growth of planetesimals by such small particles would be excruciatingly slow, $t_{\text{gr}} \sim t_0/\tau_s \sim 50 \text{ Myr}$ for the parameters listed in Equation (5), far exceeding the lifetime of the gas disk. A growth timescale $\lesssim 10^6 \text{ yr}$ would therefore imply a (midplane) dust-to-gas ratio $Z_{\text{peb}} \sim 1$, which seems unlikely for small τ_s particles. In summary, it is unlikely that TNOs could accrete pebbles from an inward-drifting pebble stream in the standard, laminar disk model.

In addition, pebble accretion in laminar disk is lossy (Ormel 2017; Lin et al. 2018). In the scenario where the birth ring is supported by pressure, all pebbles can (eventually) be accreted. That is, the efficiency is near 100%. This contrasts with the smooth disk scenario, where pebbles that fail to be accreted are lost. Consequently, the total mass in pebbles *required* for accretion, m_{needed} , exceeds the mass in pebbles actually accreted (m_{peb}). In a laminar disk, we can estimate m_{needed} as

$$\begin{aligned} m_{\text{needed}} &\sim 2\pi r v_r \rho_{\text{peb}} H_{\text{peb}} t \sim 4\pi M_{\odot} \eta h \tau_s \sqrt{\frac{\alpha_z}{\alpha_z + \tau_s}} \frac{t}{t_0} \\ &\sim 1.4 \times 10^3 m_{\oplus} \left(\frac{h}{0.07} \right)^3 \left(\frac{\alpha_z/\tau_s}{1} \right)^{1/2} \frac{t}{t_0/\tau_s} \end{aligned} \quad (21)$$

where t is the duration of the pebble accretion, $H_{\text{peb}} = hr \sqrt{\alpha_z/(\alpha_z + \tau_s)}$ the pebble scaleheight (Dubrulle et al. 1995), and ρ_{peb} the pebble density for which we substituted Equation (5). In the second line, we used again $t \sim t_0/\tau$. Equation (21) highlights that a great number of pebbles—far exceeding the mass actually accreted (m_{peb})—is required, underscoring the inefficiency of pebble accretion in the primordial belt in a laminar setting. For small τ_s , the problem is that pebbles are not sufficiently concentrated in the midplane, whereas large τ_s implies a short duration of pebbles in the primordial belt.

⁹ This is the rms particle-particle relative velocity between two particles in the inertial range. The rms particle-planetesimal relative velocity for $\tau_s < 1$ particles is $\Delta v = \mathcal{M}c_s$.

All these concerns would alleviate considerably when the disk is colder. Expressed in terms of the disk aspect ratio ($h \propto T^{1/2}$), $\eta \propto h^2$ and therefore $\tau_s \propto \sigma^{-3} \propto h^{-6}$ from Equation (15). For example, when $h = 0.05$ (about 35 K at 20 au; see Equation (7)), $\tau_s \approx 6 \times 10^{-3}$, a factor of 10 increase, the drift timescale reduces by a factor of 4 compared to Equation (19), the growth timescale may fall below the lifetime of the disk, and the required pebble mass m_{needed} to values below $500 m_{\oplus}$. These numbers are within the realm of pebble accretion models (Lambrechts et al. 2019) albeit on the high side. A question that arises, however, is where these $500 m_{\oplus}$ in solids would end up, as the Solar System's giant planets, while enriched, are not dominated in metals.

5. Discussion

5.1. Pebble accretion in the cold classical belt?

The absence of $H_r < 5$ bodies in the cold classical belt strongly suggests that pebble accretion did not play a significant role in the formation of these objects. Compared to the primordial belt, which has an estimated mass of $\sim 20 m_{\oplus}$, the cold belt is four orders of magnitude less massive (Kavelaars et al. 2020). If accretion is local, as in the turbulent model, the far fewer number of bodies in the cold belt imply a significantly reduced pebble density (ρ_{peb}), which would make growth by pebble accretion ineffective. Alternatively, in the laminar scenario the number of pebbles that could have drifted through would be much greater. However, the drawbacks outlined in the previous section would only intensify. The greater distance of the cold belt (~ 40 au instead of ~ 20 au) and the correspondingly higher aspect ratio h , would increase the characteristic growth timescale t_0/τ_s , the pebble drift timescale t_{drift} (Equation (19)) and the total mass of the pebble reservoir (m_{needed} ; Equation (21)) to levels that become unrealistic. In addition, the conditions in the cold belt may have been such to inherently prevent pebble accretion from being triggered, i.e., $m \ll m_*$. The brightest cold classical is the binary (79360) Sila–Nunam (Huang et al. 2022) with an estimated system mass of 1.1×10^{22} g (Grundy et al. 2012) ($D \approx 280$ km). From Figure 7, it is evident that these bodies barely fulfill the criterion for pebble accretion. While the specific conditions in the cold classical belt may differ, the parameters involved in setting the value of m_* do not help. First, the higher η would increase m_* and, second, a lower τ_s , while it would bring down m_* , would slow down pebble accretion to levels that make it unviable. In conclusion, it is highly improbable that the bodies in the cold belt grew substantially from a passing swarm of pebbles.

5.2. Formation time constraints

Recently, Cañas et al. (2024) also investigated the growth of TNOs by pebble accretion. Their approach is complementary to ours. In particular, their study emphasizes the composition and internal density of TNOs. A key constraint is that "small" TNOs of radius 50–100 km could not have formed too quickly as radiogenic heating—primarily Al-26 decay at a half-life of 0.7 Myr (Norris et al. 1983)—would have molten these bodies and reduced their porosity. This outcome contrasts observations, which indicates that these TNOs have retained significant porosity (Bierson & Nimmo 2019).

Cañas et al. (2024) addressed this conundrum by hypothesizing that the initial distribution of TNOs formed through streaming instabilities dominated by large, ice-rich pebbles. Processes as photodesorption could have resulted in a compositional dichotomy where ice is effectively transferred to the larger parti-

cles, which settled to the midplane layers that were shielded from stellar UV irradiation. Cañas et al. (2024) argue that streaming instability would favor the larger, ice-rich pebbles over the smaller Al-26 rich ones. Hence, the first generation of planetesimals were low in Al-26 and the early heating problem outlined by Bierson & Nimmo (2019) is avoided. Subsequently, these bodies accreted smaller, water-poor and denser pebbles over much longer timescales, when heating by Al-26 decay is less significant.

Alternatively, TNOs may have formed late, only after several half-lives of Al-26 (Bierson & Nimmo 2019). This scenario implies that the conditions necessary for the primordial belt to form only emerged after several Myr. Subsequently, pebble accretion could proceed without significant heating constraints. However, it would then be limited by the remaining time of the gaseous disk. Formation in a ring setting, where accretion timescales are short (~ 1 Myr) is then the preferred scenario.

5.3. Did TNOs form by Planetesimal Accretion?

An alternative to formation of TNOs by pebbles is growth among the planetesimal population itself (e.g., Kenyon & Bromley 2004). In this scenario accretion first proceeds through a rapid runaway growth phase (Wetherill & Stewart 1989), followed by a slower oligarchic growth phase (Kokubo & Ida 1998). Runaway growth conditions require that the initial population of bodies of mass m_0 is dynamically quiescent (zero eccentricity), such that gravitational focusing becomes more effective for higher mass bodies. During runaway growth, a small number of bodies of mass much larger than m_0 emerge on a timescale that is a fraction of the collision timescale among the initial population, $t_{\text{col},0}$. The distribution evolves into a mass spectrum $dN/dm \propto m^{-2.5}$ (Kokubo & Ida 1996; Barnes et al. 2009; Ormel et al. 2010b; Morishima et al. 2013). During the subsequent oligarchic growth, the most massive bodies separate from the continuous mass distribution, resulting in a flattening of the cumulative mass function. However, these oligarchs dynamically excite the planetesimal population, increasing their eccentricities and significantly slowing down growth.

The similarity of the TNO mass distribution to a $p = -2.5$ power-law (see Figure 2) has been interpreted as evidence for a runaway growth origin (Ormel et al. 2010a; Kenyon & Bromley 2012; Morishima 2017). For the tapered-exponential distribution of Equation (2), it is natural to let m_0 coincide with the mass scale where most of the population mass resides, i.e., $m_0 \sim 4m_{\text{brk}} \approx 10^{21}$ g (see Appendix A), corresponding to a radius of about 50 km. The initial collision timescale then evaluates

$$\begin{aligned} t_{\text{col},0} &\sim \frac{\rho_{\bullet} R}{\Sigma_{\text{pltm}} \Omega} = \frac{2\pi r W_r \rho_{\bullet} R}{(Gm_{\odot}/r^3)^{1/2} m_{\text{PB}}} \\ &= 67 \text{ Myr} \left(\frac{m_{\text{PB}}}{20 m_{\oplus}} \right)^{-1} \left(\frac{r}{20 \text{ au}} \right)^{7/2} \frac{W_r/r}{0.2} \frac{\rho_{\bullet}}{1 \text{ g cm}^{-3}} \frac{R}{50 \text{ km}}, \end{aligned} \quad (22)$$

where m_{PB} is the mass of the primordial belt and W_r/r its fractional width. Unlike pebble accretion, planetesimal-driven growth does not need to complete before the gas disk disperses, but it must complete before the onset of the dynamical instability. The survival of the binary Jupiter Trojan Patroclus–Menoetius puts constraints on the level of dynamical interactions in the precursor primordial belt. Specifically, Nesvorný et al. (2018) find a surviving probability exponentially decaying by a factor of 10 for every 100 Myr. Studies simulating the timing of the giant planet instability are consistent with these

constraints (de Sousa et al. 2020). Thus, while these constraints limit the time for collisional processing in the primordial belt, the runaway growth phase is likely to have been sufficiently rapid (Equation (22)) to establish the $p = -2.5$ mass spectrum.

However, the TNO size distribution flattens at high mass, suggesting that the high-mass bodies (Triton, Pluto, Eris) accreted significantly more mass than their low-mass counterparts. This characteristic is a hallmark of oligarchic growth, but it could also be achieved with pebble accretion (see, e.g., the *lami-1p-himass* model in Figure 6). Oligarchic growth, however, proceeds much slower than runaway growth and it may be challenging to meet the aforementioned timescale constraints. Alternatively, the runaway growth phase could have continued until Pluto-sized bodies, resulting in a continuous $p = -2.5$ mass spectrum, but with the subsequent stochastic implantation retaining a much higher fraction of TNO dwarf planets. In order to determine whether planetesimal or pebble accretion was the dominant formation mechanism, future simulations are needed to evaluate the scenarios under equivalent conditions. These efforts would greatly benefit from a more extensive and complete sample of TNOs.

5.4. The definition of a dwarf planet

The International Astronomical Union (IAU) defines a dwarf planet as “an object in orbit around the Sun that is large enough to pull itself into a nearly round shape but has not been able to clear its orbit of debris”¹⁰. While planetesimals formed through SI can exhibit irregular shapes (as exemplified by Arrokoth’s bi-lobed structure), significant pebble accretion would naturally lead to more spherical bodies through the slow settling of material and the isotropy of the accretion process. Therefore, a body grown by pebble accretion with $m_{\text{final}} \gg m_{\text{init}}$ is expected to have a nearly round shape. Specifically, if we set the mass gain factor at 10, $m_{\text{final}} = 10m_{\text{init}}$, our simulations indicate that TNOs with masses greater than $\sim 10^{-4}m_{\oplus}$ (or 6×10^{23} g, comparable to Orcus) would fulfill the IAU requirement of dwarf planet (Figure 7). Future stellar occultations of TNOs are essential to test this hypothesis.

6. Conclusions

In this study, we investigated a scenario in which high-mass trans-Neptunian objects (TNOs) accreted pebbles before being implanted into their current locations. The characteristics of the TNO size distribution suggest that the dynamically hot bodies featured processing at the high-mass end, where the distribution significantly flattens (see Figure 2). This finding aligns with the pebble accretion mechanism, which operates preferentially on the most massive bodies—those exceeding the critical mass threshold m_* (Figure 4). Focusing on a carefully selected sample of dynamically hot TNOs within 48 au, for which we argue the population is complete ($H_r < 5$ for bodies in the Minor Planet Survey and $H_r < 8.3$ for bodies in OSSOS++), we performed an MCMC analysis to best reproduce the observed present-day size distribution. This analysis allowed us to constrain the key parameters that describe the pebble accretion process, specifically the pebbles aerodynamic size (τ_s) and the pebble-planetesimal velocity (Δv).

Our main conclusions are the following:

1. The TNO size distribution tightly constrains the combination of the TNO-pebble relative velocity Δv and pebble aero-

dynamic size τ_s in the primordial belt (Table 2 and Equation (15)). This corresponding threshold mass m_* , implies that bodies above $\sim 10^{22}$ g have enjoyed significant growth by pebble accretion (see Figure 7). While simulations featuring τ_s smaller than $\sim 10^{-3}$ would formally fit the data, they imply very long accretion times, which rival the lifetime of the disk. Bodies exceeding m_* increase their mass by many tenfolds, becoming Dwarf Planets (see Figure 7).

2. The data can be fitted with either a laminar or a turbulent velocity field. There is at present no evidence for a second pebble size. This stems mainly from the lack of bodies in the high-mass tail of the TNO distribution, which render the fit insensitive to this part.
3. TNOs likely did not form in a laminar disk. In such an environment, the radial pressure gradient would imply the particle aerodynamic size $\tau_s \lesssim 10^{-3}$. Such small pebbles couple too well to the gas for pebble accretion to be effective. It would have made the process too slow in comparison to disk lifetimes. In addition, pebble accretion in smooth disks would put enormous demands on the total mass of pebbles that must have passed through the primordial belt (Equation (21)); most of which do not get accreted). These concerns would be mitigated, however, in a cold disk environment.
4. Most likely, pebble accretion proceeded locally, under conditions where pebbles are entrained by pressure and could not escape from the birth ring. In this case, $\eta = 0$ and the relative velocity is due to turbulence. These conditions would resemble the observed continuum mm-emission from continuum rings by ALMA. The inferred (σ, τ_s) relation constrained from this work can be combined with the constraints the extent of the rings provide to give a preferred pebble aerodynamic size of $\tau_s \approx 10^{-2}$. Pebble accretion could have been complete in ~ 0.1 –1 Myr.

Future surveys like CLASSY (Fraser et al. 2022) and especially the advent of the Vera C. Rubin Observatory (LSST, Collaboration et al. 2021) will greatly expand the TNO inventory by ten folds. This will allow us to further constrain the pebble accretion process and deepen our understanding of planet formation in greater detail.

Acknowledgements. This work is supported by the National Natural Science Foundation of China under grant No. 12250610189, 12233004, and 12473065. Y.H. acknowledges funding support from Tsinghua University and National Observatory of Japan. The authors appreciate the referee for a thoughtful report, B. Gladman and E. Kokubo for useful discussions, and J.-M. Petit for providing the original OSSOS++ data.

References

- Abod, C. P., Simon, J. B., Li, R., et al. 2019, *ApJ*, 883, 192
 Adams, E. R., Gulbis, A. A. S., Elliot, J. L., et al. 2014, *AJ*, 148, 55
 Agnor, C. B. & Hamilton, D. P. 2006, *Nature*, 441, 192
 Andrews, S. M., Huang, J., Pérez, L. M., et al. 2018, *ApJ*, 869, L41
 Bae, J., Isella, A., Zhu, Z., et al. 2023, in *Astronomical Society of the Pacific Conference Series*, Vol. 534, *Astronomical Society of the Pacific Conference Series*, ed. S. Inutsuka, Y. Aikawa, T. Muto, K. Tomida, & M. Tamura, 423
 Bannister, M. T., Gladman, B. J., Kavelaars, J. J., et al. 2018, *ApJS*, 236, 18
 Barnes, R., Quinn, T. R., Lissauer, J. J., & Richardson, D. C. 2009, *Icarus*, 203, 626
 Bernardinelli, P. H., Bernstein, G. M., Sako, M., et al. 2022, *ApJS*, 258, 41
 Bierson, C. J. & Nimmo, F. 2019, *Icarus*, 326, 10
 Birnstiel, T., Ormel, C. W., & Dullemond, C. P. 2011, *A&A*, 525, A11
 Brown, M. E. 2008, *The largest Kuiper belt objects*, ed. M. A. Barucci, H. Boehnhardt, D. P. Cruikshank, & A. Morbidelli, *The Solar System Beyond Neptune* (Tucson: University of Arizona Press)
 Brozović, M. & Jacobson, R. A. 2024, *AJ*, 167, 256
 Cañas, M. H., Lyra, W., Carrera, D., et al. 2024, *PSJ*, 5, 55

¹⁰ <https://www.iau.org/public/themes/pluto/>

- Canup, R. M. 2005, *Science*, 307, 546
- Chen, Y.-T., Gladman, B., Volk, K., et al. 2019, *AJ*, 158, 214
- Collaboration, V. C. R. O. L. S. S. S., Jones, R. L., Bannister, M. T., et al. 2021, *Bulletin of the AAS*, 53
- Cuzzi, J. N., Hogan, R. C., Paque, J. M., & Dobrovolskis, A. R. 2001, *ApJ*, 546, 496
- de Sousa, R. R., Morbidelli, A., Raymond, S. N., et al. 2020, *Icarus*, 339, 113605
- Doressoundiram, A., Peixinho, N., Bergh, C. d., et al. 2002, *AJ*, 124, 2279
- Drązkowska, J., Bitsch, B., Lambrechts, M., et al. 2023, in *Astronomical Society of the Pacific Conference Series*, Vol. 534, *Astronomical Society of the Pacific Conference Series*, ed. S. Inutsuka, Y. Aikawa, T. Muto, K. Tomida, & M. Tamura, 717
- Dubrulle, B., Morfill, G., & Sterzik, M. 1995, *Icarus*, 114, 237
- Fernández-Valenzuela, E., Pinilla-Alonso, N., Stansberry, J., et al. 2021, *PSJ*, 2, 10
- Foreman-Mackey, D., Hogg, D. W., Lang, D., & Goodman, J. 2013, *PASP*, 125, 306
- Fraser, W., Lawler, S., Ashton, E., et al. 2022, 54, 414.01
- Fraser, W. C., Brown, M. E., Morbidelli, A., Parker, A., & Batygin, K. 2014, *ApJ*, 782, 100
- Gladman, B., Marsden, B. G., & Vanlaerhoven, C. 2008, *The Solar System Beyond Neptune*, Vol. 43, *Nomenclature in the Outer Solar System*, ed. M. A. Barucci, H. Boehnhardt, D. P. Cruikshank, & A. Morbidelli (Tucson: University of Arizona Press)
- Gomes, R. S. 2003, *Icarus*, 161, 404
- Grundy, W., Benecchi, S., Rabinowitz, D., et al. 2012, *Icarus*, 220, 74
- Grundy, W. M., Noll, K. S., Roe, H. G., et al. 2019, *Icarus*, 334, 62
- Güttler, C., Blum, J., Zsom, A., Ormel, C. W., & Dullemond, C. P. 2010, *A&A*, 513, A56
- Huang, Y. 2023, *Dynamics of transneptunian objects under the influence of a rogue planet*, PhD Thesis (Vancouver, Canada: University of British Columbia)
- Huang, Y., Gladman, B., & Volk, K. 2022, *ApJS*, 259, 54
- Ida, S., Guillot, T., & Morbidelli, A. 2008, *ApJ*, 686, 1292
- Ida, S. & Makino, J. 1993, *Icarus*, 106, 210
- Jeffreys, H. 1998, *The theory of probability* (Oxford University Press)
- Jiang, H., Macías, E., Guerra-Alvarado, O. M., & Carrasco-González, C. 2024, *A&A*, 682, A32
- Jones, R., Gladman, B., Petit, J.-M., et al. 2006, *Icarus*, 185, 508
- Kavelaars, J., Lawler, S. M., Bannister, M. T., & Shankman, C. 2020, *The Trans-Neptunian Solar System*, Vol. astro-ph.EP, *Perspectives on the distribution of orbits of distant Trans-Neptunian objects* (Elsevier)
- Kavelaars, J. J., Petit, J.-M., Gladman, B., et al. 2021, *ApJ*, 920, L28
- Kenyon, S. J. & Bromley, B. C. 2004, *AJ*, 128, 1916
- Kenyon, S. J. & Bromley, B. C. 2012, *AJ*, 143, 63
- Kokubo, E. & Ida, S. 1996, *Icarus*, 123, 180
- Kokubo, E. & Ida, S. 1998, *Icarus*, 131, 171
- Lacerda, P. & Jewitt, D. C. 2007, *AJ*, 133, 1393
- Lambrechts, M. & Johansen, A. 2012, *A&A*, 544, A32
- Lambrechts, M., Morbidelli, A., Jacobson, S. A., et al. 2019, *A&A*, 627, A83
- Levison, H. F., Morbidelli, A., VanLaerhoven, C., Gomes, R., & Tsiganis, K. 2008, *Icarus*, 196, 258
- Lin, J. W., Lee, E. J., & Chiang, E. 2018, *MNRAS*, 480, 4338
- Liu, B. & Ji, J. 2020, *Research in Astronomy and Astrophysics*, 20, 164
- Liu, B. & Ormel, C. W. 2018, *A&A*, 615, A138
- Lyra, W., Johansen, A., Cañas, M. H., & Yang, C.-C. 2023, *ApJ*, 946, 60
- Lyra, W., Youdin, A. N., & Johansen, A. 2021, *Icarus*, 356, 113831
- Malhotra, R. 1993, *Nature*, 365, 819
- McKinnon, W. B., Richardson, D. C., Marohnic, J. C., et al. 2020, *Science*, 367, aay6620
- Morbidelli, A., Levison, H. F., Tsiganis, K., & Gomes, R. 2005, *Nature*, 435, 462
- Morgado, B. E., Sicardy, B., Braga-Ribas, F., et al. 2023, *Nature*, 614, 239
- Morishima, R. 2017, *Icarus*, 281, 459
- Morishima, R., Golabek, G. J., & Samuel, H. 2013, *Earth and Planetary Science Letters*, 366, 6
- Müller, T., Lellouch, E., & Fornasier, S. 2020, *The Trans-Neptunian Solar System*, 153
- Napier, K. J., Lin, H. W., Gerdes, D. W., et al. 2024, *PSJ*, 5, 50
- Nesvorný, D. 2015, *AJ*, 150, 73
- Nesvorný, D., Li, R., Youdin, A. N., Simon, J. B., & Grundy, W. M. 2019, *Nature Astronomy*, 3, 808
- Nesvorný, D., Vokrouhlický, D., Bottke, W. F., & Levison, H. F. 2018, *Nature Astronomy*, 2, 878
- Nesvorný, D., Vokrouhlický, D., & Morbidelli, A. 2013, *ApJ*, 768, 45
- Nesvorný, D., Vokrouhlický, D., & Roig, F. 2016, *ApJ*, 827, L35
- Nesvorný, D., Youdin, A. N., & Richardson, D. C. 2010, *AJ*, 140, 785
- Noll, K. S., Grundy, W. M., Nesvorný, D., & Thirouin, A. 2020, *Trans-Neptunian binaries (2018)*, ed. D. Prrialnik, M. A. Barucci, & L. A. Young, *The Trans-Neptunian Solar System* (Amsterdam: Elsevier Science Publishing)
- Norris, T. L., Gancarz, A. J., Rokop, D. J., & Thomas, K. W. 1983, *Lunar and Planetary Science Conference Proceedings*, 88, B331
- Ormel, C. W. 2017, in *Astrophysics and Space Science Library*, Vol. 445, *Astrophysics and Space Science Library*, ed. M. Pessah & O. Gressel, 197
- Ormel, C. W. & Cuzzi, J. N. 2007, *A&A*, 466, 413
- Ormel, C. W., Dullemond, C. P., & Spaans, M. 2010a, *ApJ*, 714, L103
- Ormel, C. W., Dullemond, C. P., & Spaans, M. 2010b, *Icarus*, 210, 507
- Ormel, C. W. & Klahr, H. H. 2010, *A&A*, 520, A43
- Ormel, C. W. & Liu, B. 2018, *A&A*, 615, A178
- Parker, A., Buie, M. W., Grundy, W., et al. 2018, in *AAS/Division for Planetary Sciences Meeting Abstracts*, Vol. 50, *AAS/Division for Planetary Sciences Meeting Abstracts #50*, 509.02
- Petit, J.-M., Gladman, B., Kavelaars, J. J., et al. 2023, *ApJ*, 947, L4
- Petit, J. M., Kavelaars, J. J., Gladman, B. J., et al. 2011, *AJ*, 142, 131
- Petit, J.-M., Morbidelli, A., & Valsecchi, G. B. 1999, *Icarus*, 141, 367
- Pike, R. E. & Lawler, S. M. 2017, *AJ*, 154, 171
- Pike, R. E., Proudfoot, B. C. N., Ragozzine, D., et al. 2020, *Nature Astronomy*, 4, 89
- Proudfoot, B. C. N. & Ragozzine, D. 2019, *AJ*, 157, 230
- Ragozzine, D. & Brown, M. E. 2009, *AJ*, 137, 4766
- Rosotti, G. P. 2023, *New A Rev.*, 96, 101674
- Schwamb, M. E., Fraser, W. C., Bannister, M. T., et al. 2019, *ApJS*, 243, 12
- Schäfer, U., Yang, C.-C., & Johansen, A. 2017, *A&A*, 597, A69
- Souami, D., Braga-Ribas, F., Sicardy, B., et al. 2020, *A&A*, 643, A125
- Trilling, D. E., Gerdes, D. W., Jurić, M., et al. 2024, *AJ*, 167, 132
- Trujillo, C. A. & Brown, M. E. 2002, *ApJ*, 566, L125
- Vilenius, E., Stansberry, J., Müller, T., et al. 2018, *A&A*, 618, A136
- Villenave, M., Stapelfeldt, K. R., Duchêne, G., et al. 2022, *ApJ*, 930, 11
- Visser, R. G. & Ormel, C. W. 2016, *A&A*, 586, A66
- Volk, K., Murray-Clay, R., Gladman, B., et al. 2016, *AJ*, 152, 23
- Weidenschilling, S. J. 1977, *MNRAS*, 180, 57
- Weiss, B. P., Bai, X.-N., & Fu, R. R. 2021, *Science Advances*, 7, eaba5967
- Weryk, R. J., Lilly, E., Chastel, S., et al. 2016, *arXiv [1607.04895]*
- Wetherill, G. W. & Stewart, G. R. 1989, *Icarus*, 77, 330
- Zsom, A., Ormel, C. W., Güttler, C., Blum, J., & Dullemond, C. P. 2010, *A&A*, 513, A57

Appendix A: TNO masses

Kavelaars et al. (2021) modeled the magnitude distribution of the cold belt as

$$N(< H_r) = 10^{\alpha'(H_r - H_0)} \exp[-10^{-\beta(H_r - H_B)}]. \quad (\text{A.1})$$

where H_r is the OSSOS magnitude, α' is the slope at low brightness objects, β describes the strength of the exponential tapering, which kicks in at $H_r \sim H_B$, and H_0 is a normalization parameter. If we define a mass-magnitude relation as

$$m = m_B 10^{-3H_r/5} \quad (\text{A.2})$$

we can relate the parameters appearing in Equation (A.1) to the cumulative distribution defined in Equation (2):

$$\gamma = \frac{5}{3}\beta; \quad \alpha = \frac{5}{3}\alpha'; \quad \frac{m_B}{m_{\text{brk}}} = 10^{\beta H_B/\gamma}; \quad N_{\text{pre}} = 10^{-\alpha' H_0} \left(\frac{m_B}{m_{\text{brk}}} \right)^\alpha. \quad (\text{A.3})$$

With $\alpha' = 0.4$ and $\beta = 0.252$ (Kavelaars et al. 2021), we obtain $\alpha = 0.67$ and $\gamma = 0.42$. We adopt the mass-magnitude conversion of Petit et al. (2023), where in Equation (A.2)

$$m_B = 9.685 \times 10^{23} \text{ g} \left(\frac{\rho_\bullet \nu^{-1.5}}{1 \text{ g cm}^{-3}} \right) \quad (\text{A.4})$$

with ν the albedo. For the cold belt, we take $\nu = 0.15$ and $\rho_\bullet = 1 \text{ g cm}^{-3}$ (Petit et al. 2023), and with $\beta = 0.252$ and $H_B = 8.1$ (Kavelaars et al. 2021), the breaking mass amounts to $m_{\text{brk}} = 2.3 \times 10^{20} \text{ g}$ and the prefactor (N_{pre}) for the cold belt $N_{\text{cold}} = 1.9 \times 10^4$. For reference, the total mass, integrating Equation (2), amounts to

$$m_{\text{tot}} = \frac{\Gamma[(1 - \alpha)/\gamma]}{\gamma} m_{\text{brk}} N_{\text{pre}} = 2.81 m_{\text{brk}} N_{\text{pre}}, \quad (\text{A.5})$$

which equals $2.0 \times 10^{-3} m_\oplus$ for the cold belt. Also, the characteristic mass of the population, defined as the ratio of the second-to-first moment of the mass distribution, is $m_* = 2\Gamma[(2 - \alpha)/\gamma]/\Gamma[(1 - \alpha)/\gamma] = 3.97 m_{\text{brk}}$.

For the hot belt, Petit et al. (2023) have shown that the shape of the magnitude distribution is the same as the cold belt with the number elevated by a factor 2.2. This would nevertheless amount to a different shape for the mass distribution (Equation (2)) since the albedos of the hot and cold belts differ, as is commonly assumed. Specifically, we take $\nu = 0.08$ and $\rho_\bullet = 1 \text{ g cm}^{-3}$ for bodies in P48. However, at high mass it is known that the mass-magnitude relationship represented by Equations (A.2) and (A.6) breaks (see Figure A.1). Several TNOs have mass estimates (those in P48 are listed in Table A.1) and we can use these to fit a mass-radius relationship for the high mass end:

$$m = m_{\text{tr}} 10^{-p_{\text{hm}}(H_r - H_{\text{tr}})} \quad (m > m_{\text{tr}}). \quad (\text{A.6})$$

Thus, at the point $(H_{\text{tr}}, m_{\text{tr}})$ the mass-magnitude relationship transitions from the low-mass expression (Equation (A.2)) to Equation (A.6), valid at high mass. Performing the fit, we obtain $H_{\text{tr}} = 4.12$ and $p_{\text{hm}} = 0.3638$.

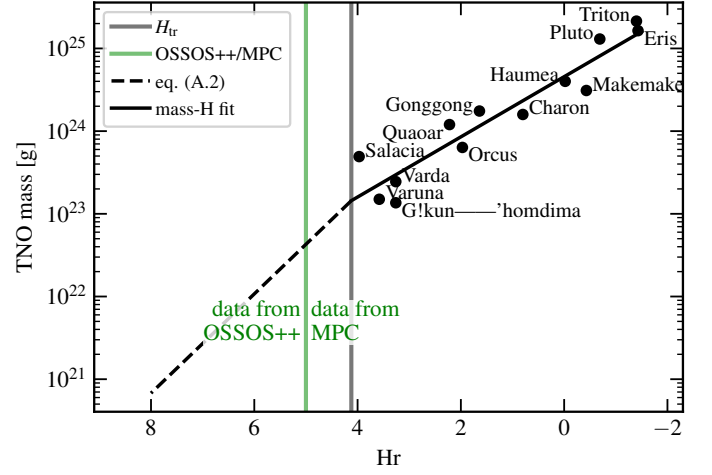


Fig. A.1. Mass-magnitude relationship for the hot main belt. At low mass we adopt the relationship given by Petit et al. (2023), Equations (A.2) and (A.6) (dashed line). At high mass we fit a power-law relationship to the TNOs for which the mass is known.

Table A.1. All TNOs in the MPC sample.

Name	H_r	a	mass	mass reference or Note	Name	H_r	a	Note
Triton	-1.40	30.07	2.14×10^{25}	¹	1995.SM55	4.43	42.14	²
Pluto	-0.69	39.40	1.30×10^{25}	Brozović & Jacobson (2024)	Chaos	4.43	46.07	
Makemake	-0.43	45.33	3.10×10^{24}	Parker et al. (2018)	2012.VR128	4.46	41.64	
Haumea	-0.02	42.90	4.00×10^{24}	Ragozzine & Brown (2009)	2005.CB79	4.50	43.22	²
Charon	0.80	39.40	1.59×10^{24}	Brozović & Jacobson (2024)	2014.OE394	4.50	46.32	
Orcus	1.97	39.24	6.35×10^{23}	Grundy et al. (2019)	2002.KX14	4.51	38.64	
Quaoar	2.22	43.19	1.20×10^{24}	Morgado et al. (2023)	2015.BZ518	4.52	46.71	
2002.AW197	3.25	47.13			2014.BV64	4.52	45.71	
Varda	3.26	45.62	2.45×10^{23}	Souami et al. (2020)	2002.XV93	4.58	39.51	
Ixion	3.27	39.41			2014.TZ85	4.59	43.83	
2002.TX300	3.31	43.58		²	2010.VK201	4.59	43.50	²
2002.MS4	3.42	41.66			Huya	4.60	39.20	
2005.RN43	3.49	41.68			1996.TO66	4.61	43.56	²
2003.AZ84	3.55	39.53			2007.JH43	4.62	39.27	
Varuna	3.58	43.08	1.50×10^{23}	Lacerda & Jewitt (2007)	2008.AP129	4.64	41.81	²
2002.UX25	3.65	43.02			2014.US224	4.64	47.14	
2005.UQ513	3.72	43.62		²	2015.AJ281	4.67	43.15	²
2004.GV9	3.77	41.74			2014.FT71	4.69	43.34	
2003.VS2	3.79	39.70			2002.XW93	4.70	37.67	
2003.OP32	3.80	43.30		²	2014.UM33	4.71	43.35	
2010.KZ39	3.82	45.01			Lempo	4.74	39.80	
2005.RR43	3.94	43.56		²	2014.BZ57	4.75	42.79	
Salacia	3.97	42.24	4.92×10^{23}	Grundy et al. (2019)	2014.HZ199	4.76	42.92	²
2004.XA192	4.02	47.44			2014.VU37	4.76	40.97	
2013.FZ27	4.06	47.93			2014.JR80	4.77	39.39	
2003.UZ413	4.09	39.48			2011.OA60	4.77	40.80	
2004.TY364	4.13	39.15			2013.JW63	4.80	45.42	
2017.OF69	4.14	39.47			2014.XY40	4.84	47.53	
2004.UX10	4.18	39.29			2014.JP80	4.85	39.45	
2004.NT33	4.22	43.56			2014.WH509	4.91	44.30	
2014.WP509	4.24	45.23			2010.RO64	4.92	47.26	
2007.JJ43	4.29	47.72			2014.QW441	4.92	44.59	²
2004.PF115	4.29	39.09			2003.QW90	4.93	44.09	
2013.XC26	4.31	42.41			2014.XR40	4.93	42.79	
2014.YA50	4.33	46.28			2015.AN281	4.96	41.75	
2010.FX86	4.35	46.54			2012.VB116	4.97	47.35	
2010.OO127	4.40	42.31			2005.CA79	4.98	47.84	
2009.YE7	4.40	44.62		²	2014.QA442	4.98	43.50	
2007.XV50	4.42	46.26			2014.AM55	4.98	47.15	

Notes. ¹https://ssd.jpl.nasa.gov/sats/phys_par/; ²Haumea family members excluded from the P48 sample (Proudfoot & Ragozzine 2019).